



**HAL**  
open science

# Impact of initializing the soil with a thermally and hydrologically balanced state on subseasonal predictability

Constantin Ardilouze, Aaron Boone

► **To cite this version:**

Constantin Ardilouze, Aaron Boone. Impact of initializing the soil with a thermally and hydrologically balanced state on subseasonal predictability. *Climate Dynamics*, 2023. meteo-04313809v2

**HAL Id: meteo-04313809**

**<https://meteofrance.hal.science/meteo-04313809v2>**

Submitted on 2 Dec 2024

**HAL** is a multi-disciplinary open access archive for the deposit and dissemination of scientific research documents, whether they are published or not. The documents may come from teaching and research institutions in France or abroad, or from public or private research centers.

L'archive ouverte pluridisciplinaire **HAL**, est destinée au dépôt et à la diffusion de documents scientifiques de niveau recherche, publiés ou non, émanant des établissements d'enseignement et de recherche français ou étrangers, des laboratoires publics ou privés.

1 **Impact of initializing the soil with a thermally and**  
2 **hydrologically balanced state on subseasonal predictability**

3 **Constantin Ardilouze · Aaron A. Boone**

4  
5 Received: date / Accepted: date

6 **Abstract** Accurate soil moisture initial conditions in dynamical subseasonal forecast  
7 systems are known to improve the temperature forecast skill regionally, through more  
8 realistic water and energy fluxes at the land-atmosphere interface. Recently, results  
9 from a multi-model coordinated experiment have provided evidence of the primal  
10 contribution of the initial surface and subsurface soil temperature over the Tibetan  
11 Plateau for capturing a hemispheric scale atmospheric teleconnection leading to im-  
12 proved subseasonal forecasts. Yet, both the soil temperature and water content are  
13 key components of the soil enthalpy and we hypothesize that properly initializing  
14 one of them without modifying the other in a consistent manner can alter the soil  
15 thermal equilibrium, thereby potentially reducing the benefit of land initial condi-  
16 tions on subsequent atmospheric forecasts. This study builds on the protocol of the  
17 above-mentioned multi-model experiment, by testing three different land initialization  
18 strategies in an Earth system model. Results of this pilot study suggest that a better  
19 mass and energy balance in land initial conditions of the Tibetan Plateau triggers a  
20 wave train which propagates through the northern hemisphere mid-latitudes, result-  
21 ing in an improved large scale circulation and temperature anomalies over multiple  
22 regions of the globe. While this study is based on a single case, it strongly advocates  
23 for enhanced attention towards preserving the soil energy equilibrium at initialization  
24 to make the most of land as a driver of atmospheric extended-range predictability.

25 **Keywords** Soil enthalpy · Tibetan plateau · Subseasonal predictability · initialization ·  
26 land-atmosphere coupling · S2S · LS4P

27 **1 Introduction**

28 At the frontier between meteorological and climatic time scales, subseasonal forecast-  
29 ing, often referred to as S2S (Subseasonal to seasonal), remains a challenge for the  
30 scientific community. While ocean interannual variability is the dominant source of

31 seasonal predictability at longer lead times, a substantial number of studies have em-  
32 phasized the key role of continental surfaces in predictability at time scales between  
33 two weeks and two months (e.g. Dirmeyer et al, 2015). Soil moisture, in particular,  
34 has received special attention since the seminal work of Koster et al (2004) which  
35 identified certain regions of the globe as hotspots of soil moisture-atmosphere cou-  
36 pling. Predictability experiments using numerical models that followed this work such  
37 as GLACE2 multi-model experiment (Koster et al, 2010) and the pilot study from  
38 Douville (2010) confirmed that a realistic initialization of soil moisture in dynamic  
39 forecasting systems could improve 2-meter temperature forecasts, particularly in so-  
40 called "water-limited" semi-arid regions. The snow-atmosphere coupling, which plays  
41 a role in the surface radiation and water balance (Xu and Dirmeyer, 2013), explains  
42 the importance of snow cover initialization for subseasonal forecasting (Orsolini et al,  
43 2013). More recently, a teleconnection has been identified between the surface and  
44 subsurface ground temperature of high altitude mountains and precipitation down-  
45 stream of the flow (Xue et al, 2016, 2018). These findings set the ground for the inter-  
46 national initiative 'Impact of Initialized Land Surface Temperature and Snowpack on  
47 Subseasonal to Seasonal Prediction Project' (LS4P) (Xue et al, 2021), gathering over  
48 40 partners and more than 20 earth system models around a common experimental  
49 forecasting protocol. The phase 1 of LS4P focused on a case study, namely the impact  
50 of land surface temperature over the Tibetan Plateau (TP) in May 2003 on the sub-  
51 sequent drought (flood) occurrence south (north) of the Yangtze river basin in June  
52 2003. The experimental setup consisted in adjusting the TP land temperature at the  
53 model initialization step of the subseasonal forecast systems, so as to mitigate the May  
54 2003 surface temperature bias analyzed in a previous baseline control forecast. In this  
55 protocol, as well as in other multi-model forecast experiments implying changes in  
56 initial soil prognostic variables such as soil moisture (Koster et al, 2011; Ardilouze  
57 et al, 2017), the physical consistency between soil prognostic variables at initialization  
58 has been overlooked. Inconsistencies may trigger dramatic model-dependent adjuste-  
59 ments and partly obscure the outcome of the numerical experiments. Moreover, it  
60 prevents disentangling the respective contributions of soil temperature, soil moisture  
61 and soil enthalpy (i.e. latent energy) on land-atmosphere coupling and subsequent  
62 atmospheric response (Zhao et al, 2018). To tackle this issue, we reproduce the pro-  
63 tocol of the LS4P prediction case study with three different initialization strategies  
64 detailed in section 2, including their impact on soil variables (subsection 2.4). Results  
65 on atmospheric forecasts are commented in section 3, before a discussion section and  
66 concluding remarks.

## 67 **2 Data and methods**

### 68 **2.1 Subseasonal forecast setup**

69 The four numerical experiments of this study each consist in a 30-member ensemble  
70 re-forecast, initialized on May 1st, 2003, and run over a 61-day forecast period, hence  
71 until June 30th. They are carried out with the CNRM-CM6-1 earth system model  
72 at the standard horizontal resolution which is approximately 150 km (Voltaire et al,

2019). The land component, Interactions between the Soil Biosphere Atmosphere-  
 CNRM Total Runoff Integrating Pathways (ISBA-CTRIP: Decharme et al, 2019), is  
 included in the Externalized Surface (SURFEX: Masson et al, 2013) model and the  
 OASIS-MCT (Ocean Atmosphere Sea Ice Soil - Model Coupling Toolkit) coupler  
 designed to process heat, water and momentum exchanges at the surface (Voldoire  
 et al, 2017). Atmospheric initial conditions are directly derived from the ERA-Interim  
 re-analysis (Dee et al, 2011) while land initial conditions result from an offline 1993-  
 2016 SURFEX simulation forced by 3-hourly ERA-Interim atmospheric fields, as  
 described in Boisserie et al (2016). Similarly, the 1° ocean and sea-ice initial con-  
 ditions are derived from an ERA-Interim forced ocean run constrained towards the  
 Mercator Ocean International Glorys 2V4 reanalysis (Ferry et al, 2010). The ensemble  
 members are generated through the addition of perturbations to the atmospheric ini-  
 tial conditions. These perturbations are designed as corrections of model drift errors,  
 following the method described in Batté and Déqué (2016).

## 2.2 Soil initial state adjustments

In the soil moisture perturbation experiments referred to in the introduction, neither  
 water mass nor enthalpy of the soil are conserved during the initialization process.  
 In this pilot study, an effort is made to use a very simple adjustment methodology  
 to conserve these quantities as best as possible, or to at least have a more physically  
 consistent initial state.

The enthalpy for a soil layer ( $\text{J m}^{-2}$ ) can be defined following (Zhao et al, 2018)  
 as:

$$h = [\rho_s c_s (1 - w_{sat}) + \rho_l c_l w_l + \rho_i c_i w_i] (T - T_f) - \rho_i L_f w_i \quad (1)$$

where  $T$  represents the temperature of the soil layer (K),  $L_f$  is the specific latent  
 heat of fusion ( $\text{J kg}^{-1}$ ), and  $w_l$ ,  $w_i$  and  $w_{sat}$  represent the liquid volumetric water  
 content of the soil, the frozen water and the soil porosity, respectively ( $\text{m}^3 \text{m}^{-3}$ ).  
 The densities for liquid water, ice and soil solids are represented by  $\rho_l$ ,  $\rho_i$  and  $\rho_s$ ,  
 respectively ( $\text{kg m}^{-3}$ ), while  $c_s$ ,  $c_w$  and  $c_i$  represent the specific heat capacity of  
 the soil constituents, liquid water, and ice, respectively ( $\text{J kg}^{-1} \text{K}^{-1}$ ). The reference  
 temperature corresponds to the freezing point of liquid water,  $T_f$  (273.15 K). In Eq. 1,  
 the contribution of air in the soil pores to  $h$  has been neglected.

To compute soil water phase changes, ISBA uses the relation between the soil  
 water potential and temperature for sub-freezing conditions from (Fuchs et al, 1978):

$$\psi^* = \psi_{sat} + \frac{L_f (T - T_f)}{g T} \quad (2)$$

where  $g$  is the gravitational constant ( $\text{m s}^{-2}$ ), and  $\psi_{sat}$  represents the soil matric  
 potential at saturation (m). The potential  $\psi^*$  can be substituted in the expression for  
 the soil matric potential in order to obtain the maximum unfrozen (liquid) water  
 content at a given soil temperature. ISBA uses the pedotransfer functions by Clapp  
 and Hornberger (1978) so that

$$w_{l,\max} = w_{sat} \left( \frac{\psi^*}{\psi_{sat}} \right)^{-1/b} \quad (3)$$

where  $b$  is related to the slope of the water retention curve. This method is described in more detail in Decharme et al (2016). Finally, a minimum liquid water content,  $w_{l,\min}$  must be defined. Here, it is simply computed as a vegetation-cover weighted average between wilting point (corresponding to a matric potential of -300 m) and a value about half of wilting point. The latter value is an approximation of the minimum value in ISBA generally found in simulations owing to baresoil evaporation.

For LS4P, we first apply a temperature perturbation,  $\Delta T$ , to soil layers in a masked region. Then the soil water and ice contents are adjusted to either conserve enthalpy which corresponds to the newly imposed temperature or the soil moisture components are adjusted in order to result in a state which is closer to a thermal equilibrium (or at least what is deemed to be more physically realistic in terms of wetting-cooling or drying-warming). The four possible responses of  $h$  to the application of a  $\Delta T$  using the methodology herein can be summarized as follows:

- 1 A potentially frozen soil thaws owing to the application of a sufficiently large  $\Delta T$ . Any soil ice is simply removed thus a warming soil is becoming potentially more dry. Mass is not conserved if the original state had soil ice. Note that using the definition of enthalpy in Eq. 1,  $h$  conservation is not possible in this pathway as it changes sign.
- 2 A soil with a temperature initially above  $T_f$  cools to below freezing. As in case 1,  $h$  conservation is not possible, but mass is potentially conserved: the partitioning between frozen and unfrozen soil water is made by imposing  $w_l \leq w_{l,\max}$  where the maximum liquid water content for  $T > T_f$  is defined using Eq. 3.
- 3 Both the initial and final soil temperatures are above freezing. There is no soil ice initially so that warming/cooling correspond to drying/wetting by simple inversion of Eq. 1 for  $w_l$  using the new  $T$ . Mass is not conserved, but enthalpy is unless the final adjusted  $w_l$  value either exceeds saturation,  $w_{sat}$ , or falls below some minimum value,  $w_{l,\min}$  (described in more detail below).
- 4 Both the initial and final soil temperatures are below freezing. In a first step, the total mass is conserved but the partitioning between ice and liquid soil water is modified to conserve enthalpy. The ice content is first diagnosed under this assumption by solving Eq. 1 for  $w_i$ . The soil ice is then checked to see if it exceeds physical limits (totally frozen soil or negative soil ice). In this case, the ice is limited and liquid water is adjusted to conserve enthalpy (and mass). As in case 3, if after adjustment the liquid water exceeds physical limits, it is limited thus both mass and enthalpy conservation imbalances can occur.

These pathways are represented by arrows in the left-hand panel of the schematic shown in Fig. 1. Indeed, when the imposed temperature change  $\Delta T$  leads to the crossing of the freezing temperature threshold  $T_f$  (meaning going from sub-freezing temperatures to freezing or vice versa), the soil enthalpy can no longer be conserved using the definition of enthalpy in Eq. 1 (i.e. using a reference temperature of  $T_f$ ) together with the fact that we are attempting to preserve the temperature anomalies. Note that in reality, latent heat changes (going between frozen and unfrozen soil states) would balance input heating or cooling. The Table in Fig. 1 summarizes the four possible pathways for the LS4P<sub>phy</sub> experiment and which quantities are conserved (or not).

	Soil temperature	Soil liquid water	Soil ice
Ctrl	✗	✗	✗
LS4P <sub>t</sub>	✓	✗	✗
LS4P <sub>sm</sub>	✗	✓	✓
LS4P <sub>phy</sub>	✓	✓	✓

Table 1: List of experiments and prognostic variables which are potentially adjusted at initialization over the TP.

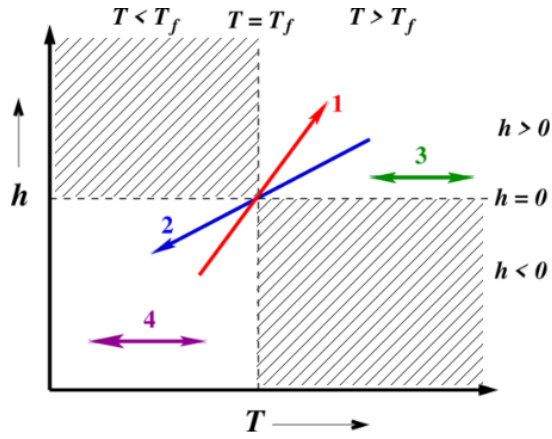
### 146 2.3 Sensitivity experiments and reference data

147 The baseline (Ctrl) experiment corresponds to the setup described in Sec. 2.1, and the  
 148 3 additional experiments only differ from the Ctrl case through changes in land initial  
 149 conditions over the TP. In LS4P<sub>t</sub>, a temperature correction mask (Fig. 2c) is applied  
 150 to the 14 soil layers of ISBA-CTRIP, corresponding to the default 10-meter soil depth.  
 151 The underlying idea of this correction is to reduce the average cold bias of the model  
 152 affecting the TP. This positive temperature mask was generated following the method  
 153 described in the section 3.2.3 of Xue et al (2021). It was calculated by taking into  
 154 account both the average cold bias over the entire TP (Fig. 2b) and the cold observed  
 155 anomaly (Fig. 2a). The LS4P<sub>phy</sub> experiment consists in adjusting soil liquid water and  
 156 ice content while applying the prescribed temperature correction, in order to impose  
 157 physical consistency and/or enthalpy conservation, to the maximum possible extent.

158 Finally, the last sensitivity experiment, LS4P<sub>sm</sub>, consists in adjusting the soil mois-  
 159 ture over the TP as in LS4P<sub>phy</sub>, but without applying the soil temperature correction.  
 160 For example, soil is dried (wetted) if a positive (negative) temperature change was  
 161 prescribed by LS4P. Thus, this experiment is somewhat akin to a GLACE type exper-  
 162 iment in that only the soil water content is modified, but in a manner consistent with  
 163 the temperature corrections (thus differing from GLACE in this respect). The aim of  
 164 LS4P<sub>sm</sub> is to provide insight on the respective contributions of the initial soil temper-  
 165 ature and soil moisture over the TP in subseasonal forecasts. Table 1 recapitulates, for  
 166 each experiment, the soil prognostic variables that are changed at initialization.

167 In this study, three reference datasets are used to evaluate our simulations. The 2-  
 168 meter temperature (t2m) is assessed against version 4 of the monthly gridded CRU-TS  
 169 dataset (Harris et al, 2020) and precipitation is evaluated using the monthly multi-  
 170 source MSWEP V2 (Beck et al, 2019) dataset. The ERA5 reanalysis (Hersbach et al,  
 171 2020) is used as the reference for atmospheric fields on standard pressure levels.  
 172 Simulation output and reference data have been re-gridded onto a common 1x1°  
 173 regular rectangular grid.

174 The comparison of 2003 subseasonal re-forecasts with observational counterparts  
 175 is based on anomalies relative to the 1993-2016 period rather than the 2003 full fields,  
 176 which is a standard bias correction strategy. In that respect, the model climatology  
 177 is computed from an extension of the Ctrl re-forecast to all the other years of the  
 178 1993-2016 period, with the same initialization day (May 1st), and following the setup  
 179 described in Sec. 2.1.



	Mass conservation	Enthalpy conservation
1	✓	✗
2	✓	✗
3	✗	✓
4	✓	✓

Fig. 1: Schematic of the four possible scenarios for soil enthalpy,  $h$ , change when initial soil temperature  $T$  is modified through the application of a temperature change in LS4P<sub>phy</sub>.  $T_f$  represents the freezing point temperature. The dashed quadrants are deemed to be physically impossible. The physically-based limits prevent enthalpy conservation in cases 1 and 2: liquid water mass is conserved for case 1 (ice is removed if initially present), and total mass is conserved for Case 2 unless physical limits of the final adjusted moisture state are exceeded. Cases 3 and 4 allow enthalpy conservation with adjustments (to soil water content) if physical limits are exceeded. If adjustments are indeed required (for example, to avoid super saturation or over-drying resulting from the first pass at enthalpy conservation), enthalpy might not be conserved.

## 180 2.4 Impact on land prognostic variables

181 To verify the validity of our setup, we first analyze the vertical profile of land prognostic  
 182 variables after one day of model integration. In Fig. 3, only the profile for the top first  
 183 meter of soil is displayed since it has an impact on land-atmosphere interactions over  
 184 the S2S timescale. Although initial soil temperature is unchanged in LS4P<sub>sm</sub> (green  
 185 line) with respect to the Ctrl (black), the temperature profile appears slightly shifted  
 186 towards higher values (Fig. 3c) due to the latent heat release owing to soil water  
 187 freezing occurring during the first steps of the model integration. This is supported  
 188 by the slightly higher ice content and lower liquid water content profiles (Fig.s 3b  
 189 and 3a, respectively) in LS4P<sub>sm</sub>, as compared to LS4P<sub>phy</sub> (orange line), despite their  
 190 identical change in initial soil water content. The difference in the temperature profile

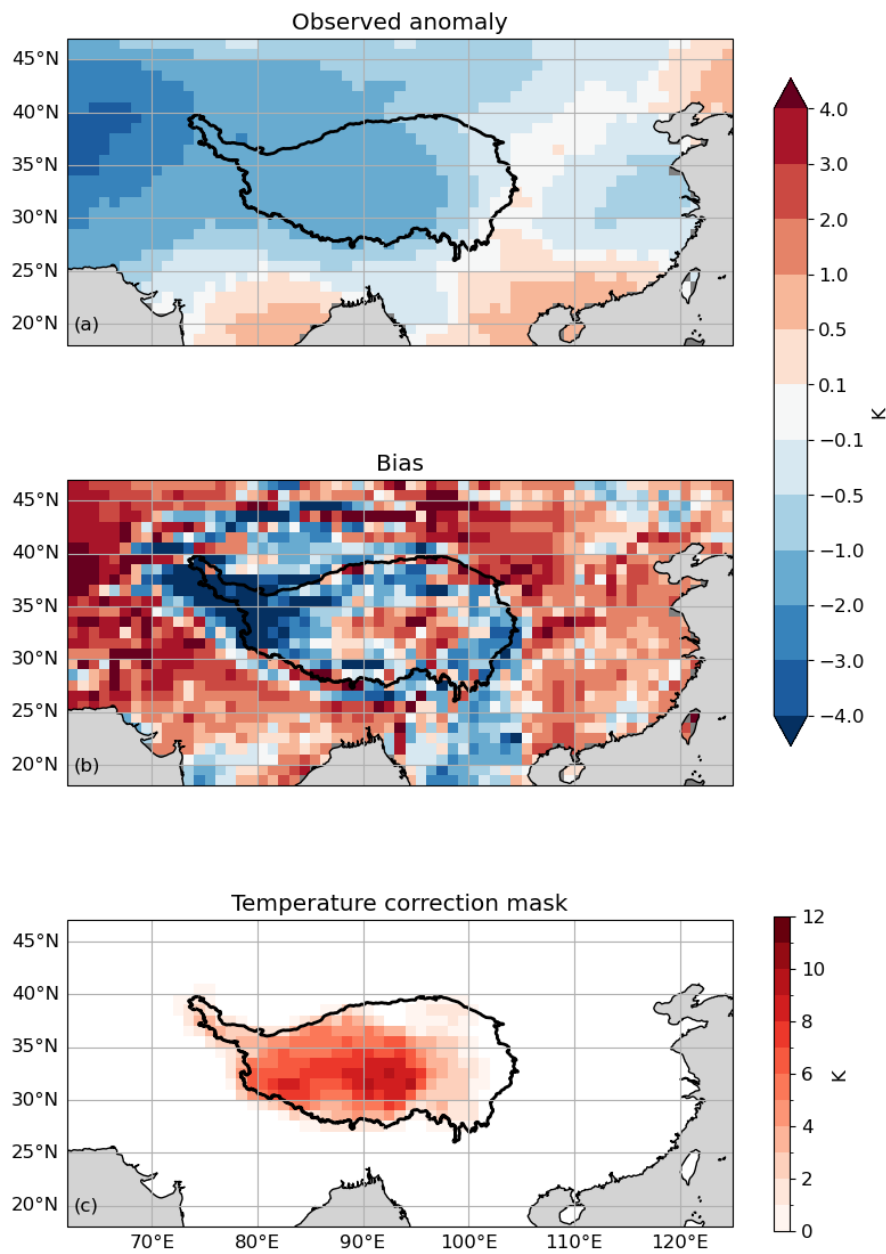


Fig. 2: (a) May 2003 observed monthly mean 2-m temperature anomaly, (b) difference between the Ctrl ensemble mean and the observation, (c) and soil temperature correction mask applied at initialisation. Unit: K



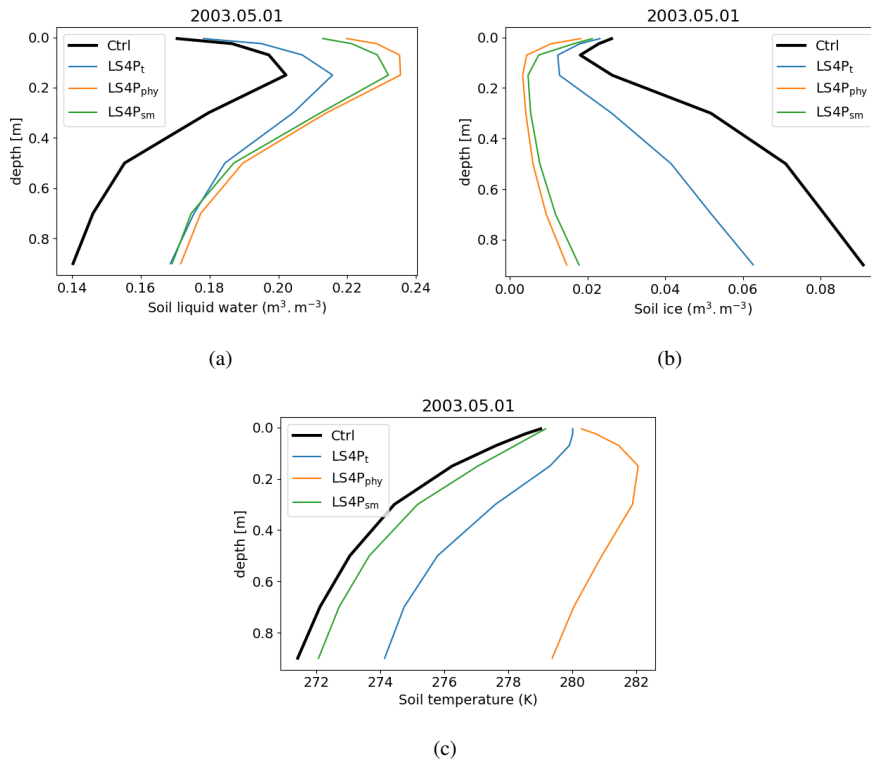


Fig. 3: Liquid water (a), ice (b) and temperature (c) soil profile averaged over the TP on May 1st 2003

191 between LS4P<sub>t</sub> (blue line) and LS4P<sub>phy</sub> (orange line) is also significant, considering  
 192 their similar initial temperature corrections. This pronounced drop in temperature  
 193 relates to soil ice thawing in LS4P<sub>t</sub>, which explains the difference with Ctrl in soil ice  
 194 profile (Fig. 3(b)) and liquid water profile (Fig. 3(a)). Thus, there is a large physical  
 195 adjustment owing to an initial state which is not in thermal equilibrium. Note that the  
 196 four temperature profiles are relatively close to each other near the surface, because  
 197 of the rapid adjustment to the overlying atmospheric conditions after the first day of  
 198 model integration.

199 Not surprisingly, the evolution of the land prognostic state variables throughout  
 200 the 2-month forecast time (Fig. 4) shows a progressive decrease of the soil ice content  
 201 in the uppermost m of the soil for the Ctrl and LS4P<sub>t</sub>, in agreement with the seasonal  
 202 atmospheric warming occurring from late spring to early summer (Fig. 4b). In re-  
 203 sponse to ice thawing, soil liquid water in LS4P<sub>t</sub> and Ctrl progressively increases with  
 204 time (Fig. 4a). While the soil moisture content remains nearly identical for LS4P<sub>sm</sub>  
 205 and LS4P<sub>phy</sub>, the latter is substantially warmer at all times, despite a decreasing trend  
 206 during the first 15 days (Fig. 4c). LS4P<sub>sm</sub> starts as cool as in Ctrl, by construction,  
 207 but ends up slightly warmer than LS4P<sub>t</sub>. This relates to the abundant soil ice in the

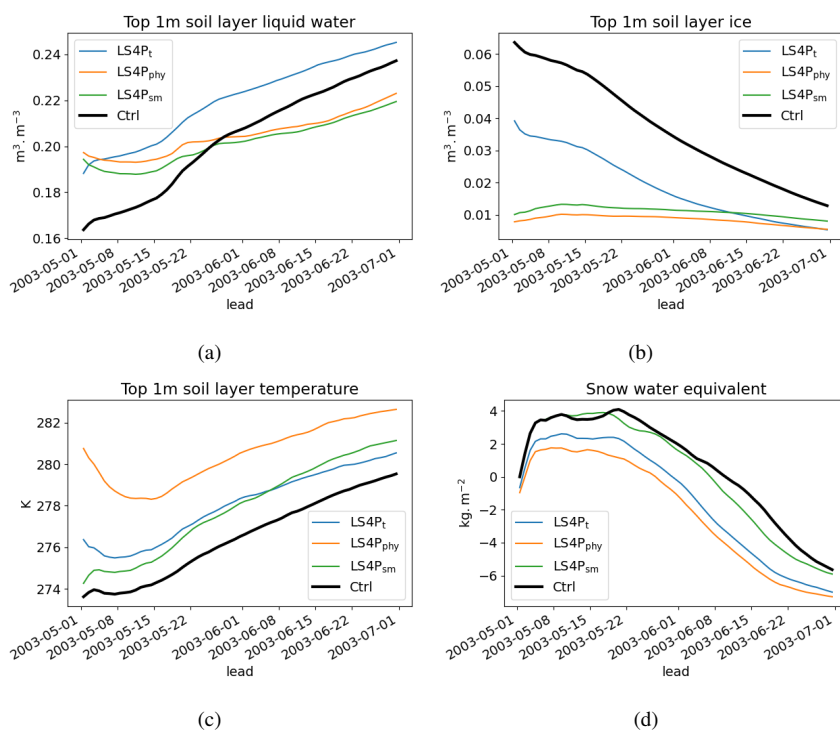


Fig. 4: Ensemble mean evolution of top 1 meter liquid water (a), ice (b), temperature (c) and snow water equivalent departure from the initial Ctrl value (d) over the TP

208 early stage of LS4P<sub>t</sub> which cools down the land surface mainly due to ice thawing in  
 209 May, and evaporation of a relatively moist soil in June. The mean snow cover over the  
 210 TP (Fig. 4d) evolves consistently, i.e. the warmer the soil, the lower the snow water  
 211 equivalent. Due to relatively cold soil conditions in LS4P<sub>sm</sub> during the first half of the  
 212 period, the average snow pack remains close to Ctrl and starts diverging afterwards.  
 213 However, although the soil becomes progressively warmer than LS4P<sub>t</sub>, the seasonal  
 214 decline of the snow cover does not catch up, because the amount of accumulated snow  
 215 at the beginning of the melting season (~ May 20th) is higher than in the other sensi-  
 216 tivity experiments. Note that in the current study, the soil states are modified while  
 217 holding the snow properties (mass, snow pack enthalpy, liquid content...) constant  
 218 between the original and perturbed setups. But owing to the feedbacks between the  
 219 soil and snow pack, we plan to investigate perturbing the snow pack properties along  
 220 with the soil in the next phase of LS4P.

### 221 3 Results

222 In this section, we analyze the atmospheric response to the land initialization strategy  
 223 over the TP. For each simulation, the ensemble mean is considered. The statistical sig-

nificance of the difference between two simulations is assessed by means of a two-sided Student's t-test for paired samples. Here, the samples correspond to the 30 ensemble members of the simulations. The null hypothesis is rejected for p-values exceeding 0.05. The comparison of the simulations with observational references is based on pattern anomaly correlation calculated over the entire northern hemisphere and 3 sub-regions: North America ( $140^{\circ}\text{W}$ - $60^{\circ}\text{W}$ , $25^{\circ}\text{N}$ - $60^{\circ}\text{N}$ ), Europe ( $15^{\circ}\text{W}$ - $45^{\circ}\text{E}$ , $30^{\circ}\text{N}$ - $70^{\circ}\text{N}$ ) and East Asia ( $80^{\circ}\text{E}$ - $140^{\circ}\text{E}$ , $20^{\circ}\text{N}$ - $55^{\circ}\text{N}$ ). The boundaries of these regions are depicted in Fig. 5(a-1). The observed anomalies are relative to the observed climatology over the 1993-2016 period, while the simulated anomalies are relative to a model climatology, derived from a full hindcast initialized on May 1st for each year of the 1993-2016 period, following the setup described in Sec. 2.1. This manner of comparing anomalies rather than full fields is a standard bias-correction procedure in the evaluation of subseasonal forecasts (e.g. Domeisen et al, 2022). Note that for assessing the statistical significance of pattern correlations, we take into account the spatial autocorrelation between adjoining grid points (Wilks, 2011). As a consequence, the effective sample size of grid points retained to compute the the t-statistic is higher for spatially heterogeneous fields (precipitation), than for smoother fields (temperature or geopotential height). Thus, for similar correlation values, the precipitation pattern correlation is more likely to be significant than the geopotential height at 500 hPa (z500) or temperature counterparts (see Table 2).

### 3.1 Evaluation of the Ctrl forecast for May and June 2003

The Ctrl re-forecast simulation is compared to observations for t2m, precipitation and mid-troposphere circulation patterns (Fig. 5). As expected, the magnitude of the June 2003 Ctrl anomaly patterns (sub-figures a-4, b-4 and c-4) are weaker than the May counterpart (a-3, b-3 and c-3) : indeed, due to the chaotic nature of the atmosphere, the forecast members tend to diverge with time and therefore the ensemble spread is larger in June than in May. The warm anomaly observed in May and June over Europe corresponds to the early stage of the extremely hot summer of 2003 (Black et al, 2004). The anomaly pattern correlations reported in Table 2 confirm that Ctrl compares remarkably well with observations in May, while to a lesser extent in June, where a spurious cool anomaly is forecast over the Iberian peninsula. The wet-North dry-South pattern, as well as the southern Europe anticyclonic blocking, are also well captured by the model in May, resulting in very high correlations for precipitation and z500. In June, a weaker, but significant signal is still found over central Europe for precipitation. More generally, the correlations drop substantially in June for most of the considered variables and regions, which is not surprising, given that the May correlations are augmented by the higher predictability of the first 10 days after initialization belonging to the meteorological predictability horizon. Over the rest of the northern hemisphere, the temperature patterns are less well captured by Ctrl with a few local exceptions like over north-west America, Asian steppes and western Africa in May. The shift from dry May to wet June anomalies north of the Gulf of Guinea is very well simulated by Ctrl. Finally, the z500 patterns are very well captured over Europe and East Asia in May but less so over North America, and conversely in June,

	2-m temperature	precipitation	z500
Northern hemisphere	M: <b>0.44</b> J: <b>0.31</b>	M: <b>0.23</b> J: <b>0.17</b>	M: <b>0.49</b> J:0.23
North America	M:0.42 J:-0.04	M: <b>0.28</b> J: <b>0.14</b>	M: <b>0.29</b> J: <b>0.46</b>
Europe	M: <b>0.59</b> J:0.28	M: <b>0.62</b> J: <b>0.23</b>	M: <b>0.89</b> J:-0.1
East Asia	M: <b>0.50</b> J:0.08	M: <b>0.14</b> J: <b>0.16</b>	M: <b>0.81</b> J:0.03

Table 2: Spatial anomaly correlation of Ctrl with Obs in May (M) and June (J) 2003. The bold font highlights positive Values which are significant at the 95% confidence level.

267 when Ctrl succeeds in simulating the positive anomaly near the West coast of North  
268 America (Fig. 5c-4).

### 269 3.2 Impact of the TP land initialization strategy

270 In May 2003 (Fig. 6a), the three perturbed simulations show a significant impact on  
271 t2m over North America. While they all tend to amplify the Ctrl warm bias from  
272 the Hudson Bay to New England, only LS4P<sub>sm</sub> and LS4P<sub>phy</sub> mitigate the cold bias  
273 over the western US. Additionally, LS4P<sub>phy</sub> simulates a cooler pattern over much of  
274 the south-east US affected by a pronounced warm bias in Ctrl. This is confirmed by  
275 the increased pattern correlation in Figure 7a. Elsewhere, none of the simulations  
276 particularly outperforms the other ones except for LS4P<sub>t</sub> which improves temperature  
277 patterns over East Europe and West Russia. At the northern hemisphere scale, all the  
278 simulations are fairly even in terms of statistically-based performance. In June 2003  
279 (Fig. 6b), the signal is weaker over America, and the simulations do not reduce the  
280 strong warm bias over Central US, a classic summer pattern in many climate models  
281 (e.g. Zhang et al, 2018). The bias is even accentuated in LS4P<sub>t</sub> and LS4P<sub>phy</sub> to a  
282 lesser extent. Over Eurasia, the three simulations show warmer t2m north east of  
283 the Caspian Sea but only LS4P<sub>phy</sub> partly compensates the cool bias over the Iberian  
284 peninsula and Central Siberia. This simulation also performs better over the TP, North  
285 China and Lapland. The t2m pattern correlation (Fig. 7b) further underscores the good  
286 performance of LS4P<sub>phy</sub> over these regions in June.

287 A similar analysis for precipitation also indicates a strong impact of our experi-  
288 mental setup in May 2003 over North America (Fig. 8a), with LS4P<sub>sm</sub> and LS4P<sub>phy</sub>  
289 showing enhanced mitigation of the wet bias over the Rockies and Great Plains. In  
290 June 2003, the signal is weak overall (Fig. 8b). However, LS4P<sub>phy</sub> indicates several  
291 local improvements. More precisely, this simulation captures a dryer pattern over cen-  
292 tral Siberia, and a wetter pattern over northern India, western Sahel and north of the  
293 Yangtze, keeping in mind that the latter regions are affected by a strong dry bias in Ctrl.  
294 The markedly wet bias over Myanmar is mitigated in both LSP<sub>t</sub> and LS4P<sub>phy</sub>. For all  
295 of the large-scale focus regions, the pattern correlations do not reveal any substantial  
296 difference between simulations (not shown). However, the aforementioned regional  
297 improvements in LS4P<sub>phy</sub> suggest a rather beneficial impact of this land initialization  
298 strategy also for the precipitation forecast. The local improvements captured nearby  
299 the Yangtze river are further commented at the end of Sec. 3.3.

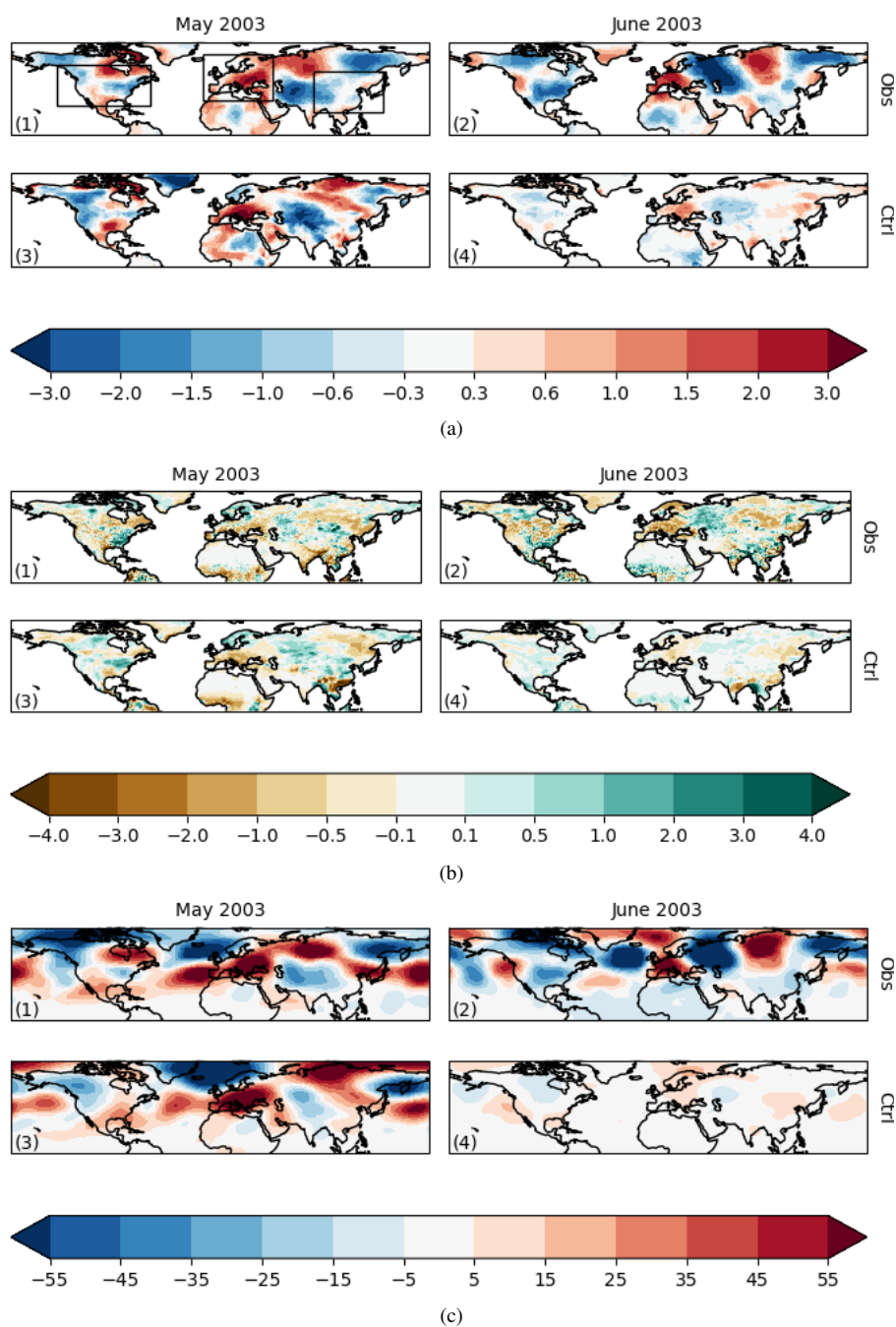


Fig. 5: Comparison of May and June 2003 observed and Ctrl anomalies for (a) 2-meter temperature in K, (b) precipitation in mm/day and (c) 500 hPa geopotential height (m)

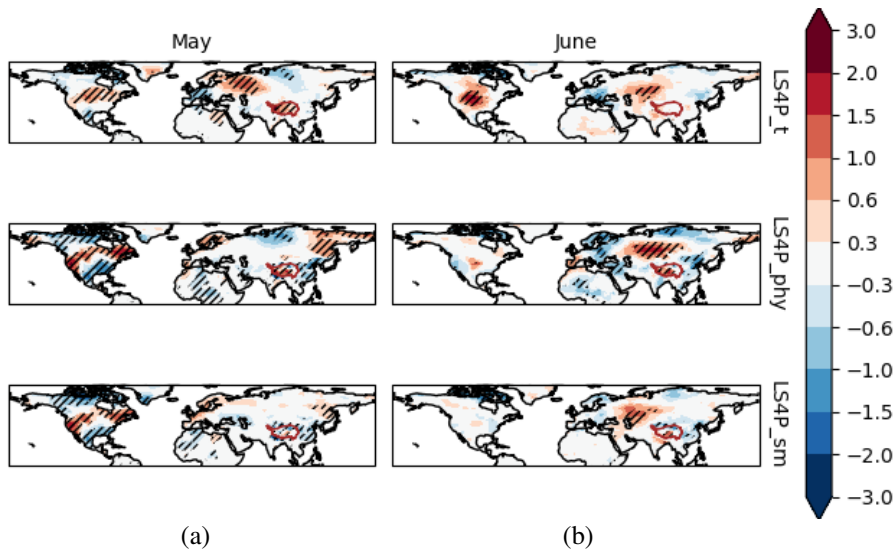


Fig. 6: (a) May 2003 and (b) June 2003 t2m differences (top row)  $LS4P_t$  minus Ctrl, (middle row)  $LS4P_{phy}$  minus Ctrl and (bottom row)  $LS4P_{sm}$  minus Ctrl, in K. Hatching indicates statistically significant values at a 95% confidence level from a 2-sided t-test.

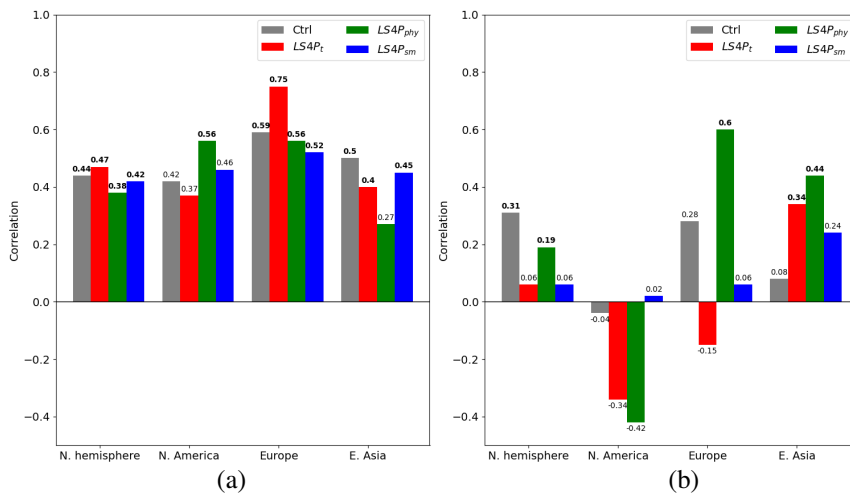


Fig. 7: (a) May 2003 and (b) June 2003 t2m anomaly pattern correlation with ERA5, by domain. Bold values are statistically significant at a 95% confidence level.

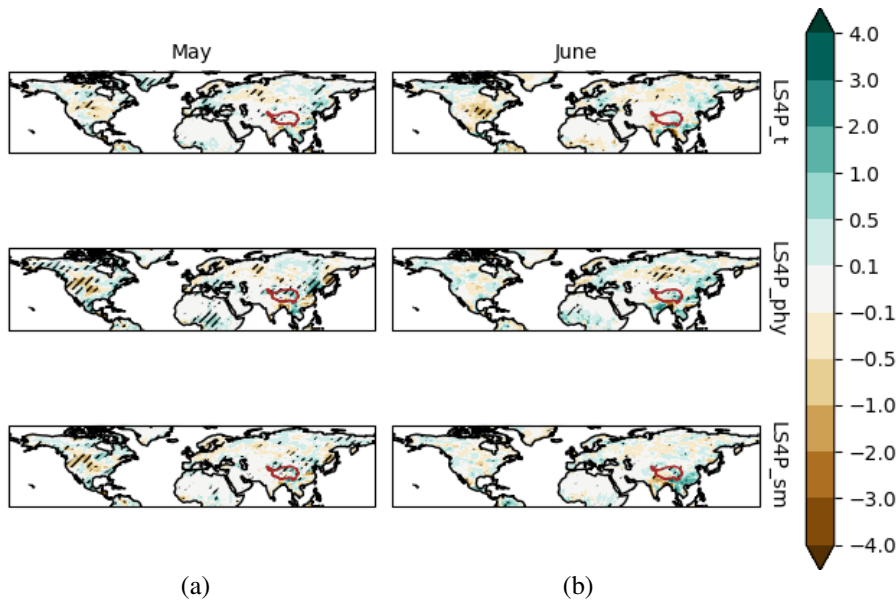


Fig. 8: As figure 6 for precipitation (unit: mm/day).

300 The  $t_2m$  and precipitation patterns described above are partly driven by changes  
 301 in the atmospheric circulation. The maps for  $z_{500}$  (Fig. 9) reveal differences with a  
 302 larger amplitude in May, especially over the western north hemisphere. Differences are  
 303 weaker for  $LS4P_t$ , though. The  $LS4P_{phy}$  map suggests a wave-like pattern. This feature  
 304 will be commented in the following section. For this simulation, the regional correlations  
 305 indicate substantially improved circulation anomalies across North America  
 306 (Fig. 10a), but no particular impact elsewhere.

307 In June (Fig. 9b), the sensitivity experiments exhibit overall less widespread  
 308 differences with respect to Ctrl. However, here again,  $LS4P_{phy}$  distinguishes itself  
 309 from the other simulations owing to a relatively marked geopotential anomaly tripole  
 310 composed by a central positive anomaly stretching across southern Siberia and two  
 311 negative anomalies over Northern Europe and, more weakly, from northern China  
 312 to north-west Pacific. This feature is also visible in  $LS4P_{sm}$  and  $LS4P_t$ , but with  
 313 barely, if at all, any significant patterns. The pattern correlations reveal that  $LS4P_{phy}$   
 314 considerably improves the circulation anomaly over both Europe, thanks to lower  
 315 geopotential height over Scandinavia, and East Asia. This result is consistent with the  
 316  $t_2m$  analysis.

317 The relatively higher performance of the Ctrl simulation over North America  
 318 in June is largely due to the successful simulation of the  $z_{500}$  positive anomaly  
 319 located near the west coast of America. A possible reason for the poorer results of the  
 320 sensitivity experiments in this respect is discussed in Sec. 4.

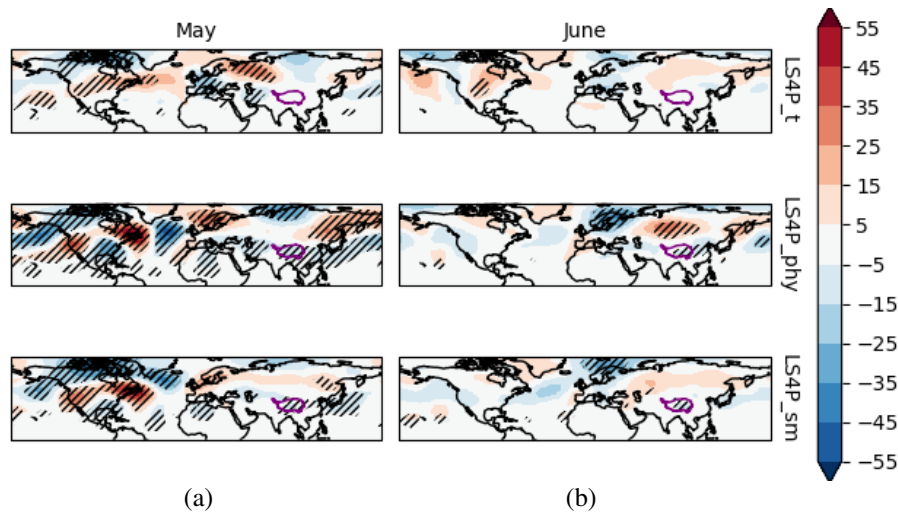


Fig. 9: As figure 6 for geopotential height at 500 hPa (unit: m).

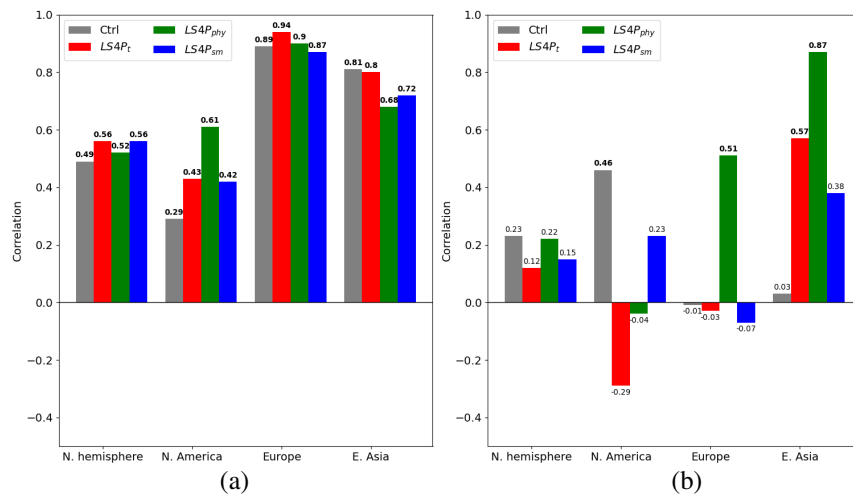


Fig. 10: (a) May 2003 and (b) June 2003 z500 anomaly pattern correlation with ERA5, by domain. Bold values are statistically significant at a 95% confidence level.

321 3.3 Description of the mechanisms involved

322 In the previous section, we identified a number of common features between the  
 323 sensitivity experiments: the adjustment of land initial conditions over the TP affects  
 324 mainly the western half of the northern hemisphere during the first month of the



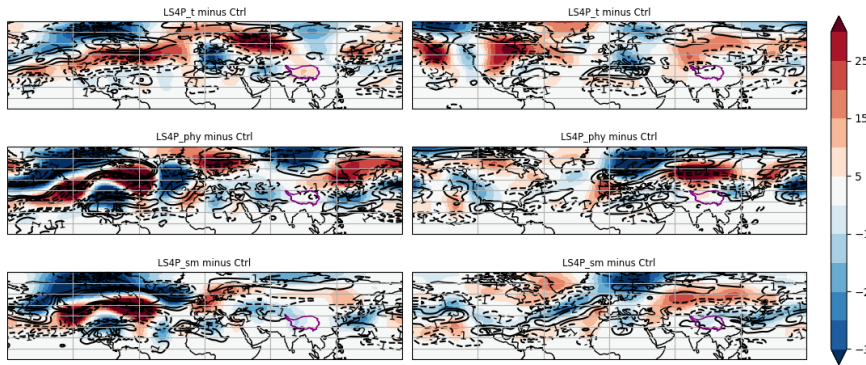


Fig. 11: May (left column) and June (right column) 2003 250 hPa geopotential height (shade) and zonal wind (contour) anomaly

325 forecast, and the eastern half during the second month, albeit less markedly. The ad-  
 326 justment strategy impacts mainly the amplitude and location of atmospheric anomaly  
 327 patterns, which translates into reduced or increased biases.

328 As suggested earlier, a striking feature of the change in z500 circulation over North  
 329 America in May 2003 for LS4P<sub>phy</sub> is a wave-like pattern. Additionally, it is remarkably  
 330 out-of-phase from the Ctrl bias pattern (the pattern correlation value between the z500  
 331 bias and the LS4P<sub>phy</sub> z500 anomaly over the North America domain is -0.74). This  
 332 is also true for LS4P<sub>sm</sub> but to a lesser extent, especially for south-East US (spatial  
 333 correlation value : -0.48). The anomaly pattern found in LS4P<sub>phy</sub> matches very well  
 334 with the Tibetan Plateau-Rocky Mountains Circumglobal (TRC) wave train identified  
 335 by Xue et al (2022) (Their Fig. 4B) and named as such in Xue et al (2023, this  
 336 issue). In June (Fig. 9b), the relative agreement between sensitivity simulations on a  
 337 geopotential anomaly tripole described earlier and stretching from Northern Europe  
 338 to Northern China suggests that the TRC, identified as a May teleconnection pattern,  
 339 can propagate in June across Eurasia. In the upper troposphere, the geopotential height  
 340 anomaly is affected consistently by the mid-troposphere (Fig. 11), and consequently,  
 341 the jet stream is shifted northwards in May over North America and in June over Asia,  
 342 with a stronger amplitude in LS4P<sub>phy</sub>.

343 In order to illustrate the dynamic propagation, we show the time evolution of  
 344 250 hPa meridional wind anomalies from Ctrl, averaged out over the 30°N-60°N  
 345 meridional cross-section (Fig. 12). The three perturbed simulations clearly show a  
 346 wave train emerging from the TP longitudes and propagating eastwards during the  
 347 first 30 days. This wave train is very weak in LS4P<sub>t</sub> and rapidly fades out while  
 348 on the other hand, it is particularly strong in LS4P<sub>phy</sub>. The attenuated wave train  
 349 re-emerges past day 40 in longitudes stretching eastwards from Central Asia to the  
 350 North Pacific. Again, it is the strongest and best established in LSP<sub>phy</sub>. The choice of a  
 351 cross section bounded between 30°N and 60°N was a trade-off to include most of the  
 352 TP and mid-latitudes, without averaging out too many opposite anomalies, that could  
 353 mask the signal. The drawback is that the wave propagation at higher latitude across

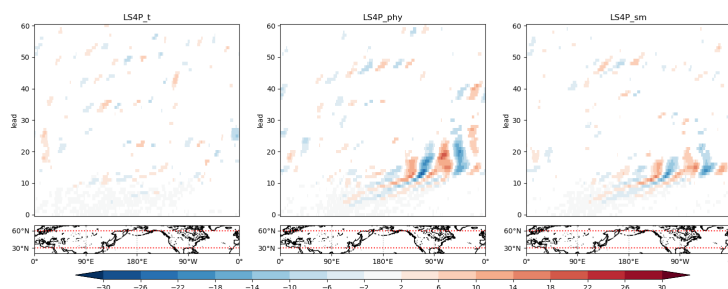


Fig. 12: Hovmöller diagrams of 250 hPa meridional wind anomaly averaged between 30°N and 60°N. Values not significant at the 95% have been set to 0.

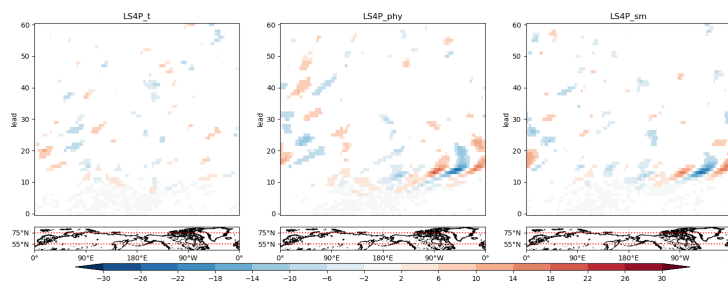


Fig. 13: As figure 12 between 55°N and 75°N.

354 northern Scandinavia and Lapland, if any, is not detectable. This could explain the  
 355 discontinuity found in wave propagation illustrated in the Hovmöller diagram between  
 356 day 25 and day 40 after initialization. A similar Hovmöller analysis has thus been  
 357 achieved for a cross section between 55°N and 75°N (Fig. 13). It reveals an eastward  
 358 wave propagation between day 25 and day 45 after initialization from the Greenwich  
 359 meridian to 80°E. This wave propagation is more pronounced in LS4P<sub>phy</sub> than in  
 360 other perturbed experiments.

361 The way land surface is initialized over the TP in early May is therefore susceptible  
 362 to trigger an extratropical circumglobal atmospheric wave train. This wave train  
 363 considerably modifies the atmospheric flow in our model for several weeks.

364 Finally, even if the impact of our experiments on continental south East Asia pre-  
 365 cipitation remains inconclusive, the potential interaction with the onset and evolution  
 366 of the East-Asian monsoon cannot be discarded, and in particular one of its main  
 367 components known as the Meiyu-Baiu front. This quasi-stationary area of intense  
 368 rainfall forms in spring at the confluence of the summer monsoon moist air south  
 369 of China and the warm dryer air to the North (e.g. Zhou et al, 2004). The location  
 370 and evolution of the Meiyu-Baiu front is governed by a wide range of factors cover-  
 371 ing multiple scales, including the thermal forcing of the TP (e.g. Liu et al, 2007),  
 372 as well as the mid-latitude westerly jet (Sampe and Xie, 2010). In this study, both  
 373 factors are impacted by the TP land initialization, and could thus change the location

374 and intensity of this front. In Fig. 14, we show the anomaly of vertically integrated  
375 moisture divergence in ERA5 and Ctrl, in order to localize the Meiyu-Baiu front.  
376 In May, Ctrl captures relatively well the divergence (convergence) anomalies in red  
377 (blue) shades, corresponding to dry (wet) spells, especially over the China sea. The  
378 strip of moisture convergence simulated south of Japan is mislocated and too zonally  
379 tilted with respect to observations. The location is partly improved in LS4P<sub>phy</sub> and  
380 LS4P<sub>sm</sub> with a south-eastward shift of this convergence front (Fig. 15a). This shift  
381 results from the change in large-scale circulation, and in particular the meridional dis-  
382 placement of the subtropical westerly jet (Sampe and Xie, 2010). More precisely, in  
383 these two simulations, the wave propagation triggers the development of a barotropic  
384 low pressure anomaly between China and Southern Japan at 500 hPa (fig. 9a), and  
385 to a lesser extent at 250 hPa, in the lee of the TP (two bottom-left maps of fig. 11).  
386 Accordingly, the subtropical westerly jet is accelerated south of this low anomaly,  
387 which favors the southwards advection of cool dry air from the mid-latitudes. Even-  
388 tually, the convergence with northward monsoonal flow is shifted further south than  
389 in the Ctrl experiment. This result is consistent with the study from Volonté et al  
390 (2022) highlighting the sensitivity of the Meiyu-Baiu front location to the transient  
391 mid-latitude weather disturbances steered by the westerly jet.

392 In June (Fig. 15b), the observed moisture divergence anomaly is rather patchy,  
393 suggesting a little organised Meiyu-Baiu front. Over China, the dry (wet) anomalies  
394 located south (north) of the Yangtze river materialize the exceptional drought (pre-  
395 cipitation) that motivated the choice of the year 2003 as the initial case study of LS4P  
396 (Xue et al, 2021). Ctrl misses these anomalies and simulates a convergence anomaly  
397 north-east of the Philippines, where observations indicate a anomalously dry pattern  
398 (red shades). This is partly improved in LS4P<sub>t</sub> and LS4P<sub>phy</sub> where dryer conditions  
399 are simulated. It is noteworthy that LS4P<sub>phy</sub> simulates a strip of enhanced moisture  
400 convergence north of the Yangtze and conversely further south. This could be related  
401 to the improved z500 circulation pointed out in Sec. 3.2, but considering the small  
402 scale of these features, verification of any relationship would require further analysis  
403 beyond the scope of the current study.

#### 404 **4 Discussion and conclusion**

405 We have revisited the LS4P exercise (Xue et al, 2021) which consists in adjusting the  
406 land initialization over the Tibetan Plateau (TP) in ESM-based late spring subseasonal  
407 forecasts. The rationale of LS4P is to mitigate the initial subsurface temperature bias  
408 affecting this high altitude region in order to make the most out of this source of  
409 extended range atmospheric predictability. In this pilot study focusing on a 2-month  
410 forecast initialized on May 1st 2003, we compared three initial adjustment strategies  
411 over the TP to assess the impact of the physical equilibrium of land initial conditions.

412 Adjusting the land initialization over the TP with more thermodynamically-  
413 balanced state variables leads to marked changes in the subsequent atmospheric  
414 response. In particular, the strategy that adjusts the soil liquid water and ice content  
415 while applying the prescribed temperature correction triggers the most effective and  
416 long-lasting atmospheric response at the hemispheric scale among the three setups.

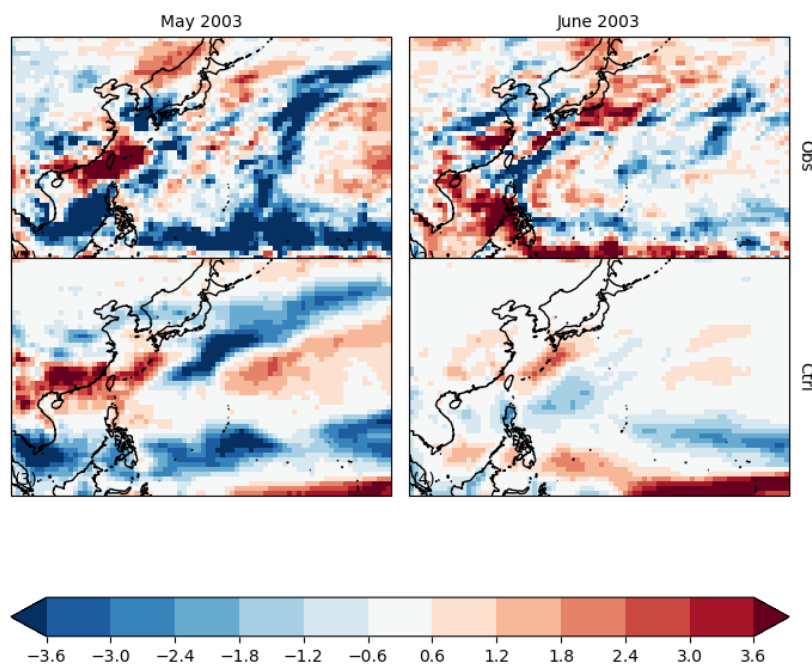


Fig. 14: Comparison of May and June 2003 observed and Ctrl anomalies for vertically integrated moisture divergence in  $\text{kg m}^{-2} \text{day}^{-1}$

417 This setup also better preserves the soil physical consistency and/or enthalpy at ini-  
 418 tialization. The atmospheric response translates into an extratropical tropospheric  
 419 wave train emerging from the TP propagating eastwards towards north America dur-  
 420 ing the first month, and more weakly to Europe and Asia during the second month. In  
 421 this study, our balanced initialization strategy improves the atmospheric circulation  
 422 pattern over North America in May and Europe and East-Asia in June, with respect  
 423 to an observational reference. It also interacts with the East-Asian monsoon flow by  
 424 changing the location and intensity of the Meiyu-Baiu front but without any noticeable  
 425 improvement.

426 Conversely, we find that neither the correction of initial land temperature alone  
 427 nor that of initial soil moisture alone has a major impact on the atmospheric response  
 428 within our model. Only the joint correction of soil moisture and temperature with  
 429 physical coherence succeeds in improving the forecast in this case study. A coordinated  
 430 multi-model exercise such as GLACE-2 or LS4P, but focused on this issue of land  
 431 physical consistency at initialization, would be required to verify if our findings  
 432 can be generalized to other models. Similarly, this paper only reports on a single  
 433 case study, and thus a way forward could be to extend this exercise over multiple  
 434 consecutive years, with an ad hoc temperature correction mask for the TP each year.  
 435 Such a multi-year reforecast is needed to evaluate the screen-level temperature and  
 436 circulation prediction skill in different regions of the Northern hemisphere. Yet, our

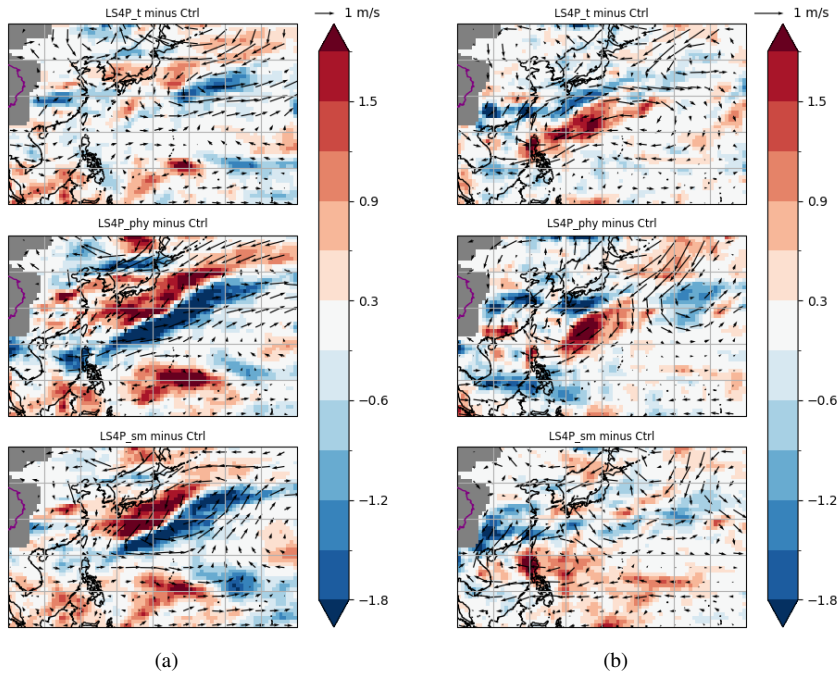


Fig. 15: (a) May and (b) June 2003 vertically integrated moisture divergence (shade) in  $\text{kg}\cdot\text{m}^{-2}\cdot\text{day}^{-1}$  and 850 hPa wind anomalies (vectors).

437 work clearly suggests the importance of preserving the land physical equilibrium in  
 438 coupled land-atmosphere numerical experiments. This question is especially acute in  
 439 subseasonal and seasonal dynamical forecast systems where the land component is  
 440 initialized in a fashion to approach observed states. This implies a direct or indirect data  
 441 assimilation system fed by superficial observations. Therefore, a joint assimilation of  
 442 both observed soil temperature and moisture while imposing a thermally-consistent  
 443 state upon initialization of the land surface could lead to improved coupled sub-  
 444 seasonal to seasonal forecasts.

445 Finally, our numerical simulations have been carried out with an interactive ocean  
 446 model in order to mimick the setup of the majority of S2S forecast systems (Vitart  
 447 et al, 2017). However, it is an exception among other contributing models in the LS4P  
 448 exercise. A similar set of experiments with prescribed sea-surface temperature would  
 449 be worth implementing to verify the robustness of our conclusions and to better  
 450 compare our results with those of other modeling systems. The limited success of  
 451 the June 2003 forecast over North America in the sensitivity experiments (Sec. 3.2)  
 452 could originate from a poor simulation of the seesaw atmospheric linkage between  
 453 the Tibetan plateau and the Rocky Mountains, as identified by Xue et al (2018). In  
 454 the second phase of the LS4P project, we plan to apply our new initialization method  
 455 over both mountain ranges simultaneously, to try and improve the model atmospheric  
 456 response.

457        Considering the increasing refinement of the physical processes simulated in land  
458 surface models, our study makes the case for particular care to be taken in the initial-  
459 ization of the land component in weather-to-seasonal forecast systems, preserving the  
460 land physical consistency to the best possible extent. Additionally, this work sheds  
461 light on the soil enthalpy which may well be a serious candidate to help reconcile the  
462 tug of war between supporters of land subsurface temperature versus root zone soil  
463 moisture as the dominant driver stemming from land in subseasonal forecasts.

**References**

- 465 Ardilouze C, Batté L, Bunzel F, Decremier D, Déqué M, Doblus-Reyes F, Douville  
466 H, Fereday D, Guemas V, MacLachlan C, Müller W, Prodhomme C (2017) Multi-  
467 model assessment of the impact of soil moisture initialization on mid-latitude  
468 summer predictability. *Climate Dynamics* 49(11-12):3959–3974
- 469 Batté L, Déqué M (2016) Randomly correcting model errors in the ARPEGE-Climate  
470 v6. 1 component of CNRM-CM: applications for seasonal forecasts. *Geoscientific  
471 Model Development* 9(6)
- 472 Beck HE, Wood EF, Pan M, Fisher CK, Miralles DG, Van Dijk AI, McVicar TR, Adler  
473 RF (2019) MSWEP V2 global 3-hourly 0.1 precipitation: methodology and quan-  
474 titative assessment. *Bulletin of the American Meteorological Society* 100(3):473–  
475 500
- 476 Black E, Blackburn M, Harrison G, Hoskins B, Methven J, et al (2004) Factors  
477 contributing to the summer 2003 european heatwave. *Weather* 59(8):217–223
- 478 Boisserie M, Decharme B, Descamps L, Arbogast P (2016) Land surface initialization  
479 strategy for a global reforecast dataset. *Quarterly Journal of the Royal Meteorolog-  
480 ical Society* 142(695):880–888
- 481 Clapp RB, Hornberger GM (1978) Empirical equations for some soil hydraulic prop-  
482 erties. *Water Resources Research* 14:601–604, DOI 10.1029/WR014i004p00601
- 483 Decharme B, Brun E, Boone A, Delire C, Le Moigne P, Morin S (2016) Impacts  
484 of snow and organic soils parameterization on northern Eurasian soil temperature  
485 profiles simulated by the ISBA land surface model. *The Cryosphere* 10(2):853–877
- 486 Decharme B, Delire C, Minvielle M, Colin J, Vergnes JP, Alias A, Saint-Martin D,  
487 Séférian R, Sénési S, Voldoire A (2019) Recent changes in the ISBA-CTrip land  
488 surface system for use in the CNRM-CM6 climate model and in global off-line  
489 hydrological applications. *Journal of Advances in Modeling Earth Systems*
- 490 Dee DP, Uppala SM, Simmons AJ, Berrisford P, Poli P, Kobayashi S, Andrae U,  
491 Balmaseda MA, Balsamo G, Bauer P, Bechtold P, Beljaars ACM, van de Berg L,  
492 Bidlot J, Bormann N, Delsol C, Dragani R, Fuentes M, Geer AJ, Haimberger L,  
493 Healy SB, Hersbach H, Hólm EV, Isaksen L, Kållberg P, Köhler M, Matricardi M,  
494 McNally AP, Monge-Sanz BM, Morcrette JJ, Park BK, Peubey C, de Rosnay P,  
495 Tavolato C, Thépaut JN, Vitart F (2011) The ERA-Interim reanalysis: configuration  
496 and performance of the data assimilation system. *Quarterly Journal of the Royal  
497 Meteorological Society* 137(656):553–597
- 498 Dirmeyer P, Peters-Lidard C, Balsamo G (2015) Land-atmosphere interactions and  
499 the water cycle. *Seamless prediction of the Earth system: from minutes to months,*  
500 edited by: Brunet, G, Jones, S, and Ruti, PM 1156
- 501 Domeisen DIV, White CJ, Afargan-Gerstman H, Ángel G Muñoz, Janiga MA, Vitart  
502 F, Wulff CO, Antoine S, Ardilouze C, Batté L, Bloomfield HC, Brayshaw DJ,  
503 Camargo SJ, Charlton-Pérez A, Collins D, Cowan T, del Mar Chaves M, Ferranti L,  
504 Gómez R, González PLM, Romero CG, Infanti JM, Karozis S, Kim H, Kolstad EW,  
505 LaJoie E, Lledó L, Magnusson L, Malguzzi P, Manrique-Suñén A, Mastrangelo D,  
506 Materia S, Medina H, Palma L, Pineda LE, Sfetsos A, Son SW, Soret A, Strazzo S,  
507 Tian D (2022) Advances in the subseasonal prediction of extreme events: Relevant  
508 case studies across the globe. *Bulletin of the American Meteorological Society*

- 509 103(6):E1473 – E1501, DOI <https://doi.org/10.1175/BAMS-D-20-0221.1>
- 510 Douville H (2010) Relative contribution of soil moisture and snow mass to seasonal  
511 climate predictability: a pilot study. *Climate Dynamics* 34(6):797–818
- 512 Ferry N, Parent L, Garric G, Barnier B, Jourdain NC, et al (2010) Mercator global  
513 Eddy permitting ocean reanalysis GLORYS1V1: Description and results. *Mercator-  
514 Ocean Quarterly Newsletter* 36:15–27
- 515 Fuchs M, Campbell GS, Papendick RI (1978) An Analysis of Sensible and Latent  
516 Heat Flow in a Partially Frozen Unsaturated Soil. *Soil Science Society of America  
517 Journal* 42:379–385, DOI 10.2136/sssaj1978.03615995004200030001x
- 518 Harris I, Osborn TJ, Jones P, Lister D (2020) Version 4 of the CRU TS monthly  
519 high-resolution gridded multivariate climate dataset. *Scientific data* 7(1):109
- 520 Hersbach H, Bell B, Berrisford P, Hirahara S, Horányi A, Muñoz-Sabater J, Nicolas  
521 J, Peubey C, Radu R, Schepers D, Simmons A, Soci C, Abdalla S, Abellan X,  
522 Balsamo G, Bechtold P, Biavati G, Bidlot J, Bonavita M, De Chiara G, Dahlgren  
523 P, Dee D, Diamantakis M, Dragani R, Flemming J, Forbes R, Fuentes M, Geer  
524 A, Haimberger L, Healy S, Hogan RJ, Hólm E, Janisková M, Keeley S, Laloyaux  
525 P, Lopez P, Lupu C, Radnoti G, de Rosnay P, Rozum I, Vamborg F, Villaume S,  
526 Thépaut JN (2020) The ERA5 global reanalysis. *Quarterly Journal of the Royal  
527 Meteorological Society* 146(730):1999–2049, DOI 10.1002/qj.3803
- 528 Koster R, Mahanama S, Yamada T, Balsamo G, Berg A, Boisserie M, Dirmeyer P,  
529 Doblas-Reyes F, Drewitt G, Gordon C, et al (2011) The second phase of the global  
530 land–atmosphere coupling experiment: soil moisture contributions to subseasonal  
531 forecast skill. *Journal of Hydrometeorology* 12(5):805–822
- 532 Koster RD, Dirmeyer PA, Guo Z, Bonan G, Chan E, Cox P, Gordon C, Kanae S,  
533 Kowalczyk E, Lawrence D, et al (2004) Regions of strong coupling between soil  
534 moisture and precipitation. *Science* 305(5687):1138–1140
- 535 Koster RD, Mahanama S, Yamada T, Balsamo G, Berg A, Boisserie M, Dirmeyer  
536 P, Doblas-Reyes F, Drewitt G, Gordon C, et al (2010) Contribution of land sur-  
537 face initialization to subseasonal forecast skill: First results from a multi-model  
538 experiment. *Geophysical Research Letters* 37(2)
- 539 Liu Y, Hoskins B, Blackburn M (2007) Impact of Tibetan orography and heating on  
540 the summer flow over Asia. *気象集誌 第 2 輯* 85:1–19
- 541 Masson V, Le Moigne P, Martin E, Faroux S, Alias A, Alkama R, Belamari S, Barbu  
542 A, Boone A, Bouyssel F, Brousseau P, Brun E, Calvet JC, Carrer D, Decharme  
543 B, Delire C, Donier S, Essaouini K, Gibelin AL, Giordani H, Habets F, Jidane M,  
544 Kerdraon G, Kourzeneva E, Lafaysse M, Lafont S, Lebeaupin Brossier C, Lemonsu  
545 A, Mahfouf JF, Marguinaud P, Mokhtari M, Morin S, Pigeon G, Salgado R, Seity  
546 Y, Taillefer F, Tanguy G, Tulet P, Vincendon B, Vionnet V, Voldoire A (2013) The  
547 SURFEXv7.2 land and ocean surface platform for coupled or offline simulation of  
548 earth surface variables and fluxes. *Geoscientific Model Development* 6(4):929–960,  
549 DOI 10.5194/gmd-6-929-2013
- 550 Orsolini Y, Senan R, Balsamo G, Doblas-Reyes F, Vitart F, Weisheimer A, Carrasco A,  
551 Benestad R (2013) Impact of snow initialization on sub-seasonal forecasts. *Climate  
552 dynamics* 41:1969–1982
- 553 Sampe T, Xie SP (2010) Large-scale dynamics of the meiyu-baiu rainband: Environ-  
554 mental forcing by the westerly jet. *Journal of Climate* 23(1):113–134



- 555 Vitart F, Ardilouze C, Bonet A, Brookshaw A, Chen M, Codorean C, Déqué M,  
556 Ferranti L, Fucile E, Fuentes M, Hendon H, Hodgson J, Kang HS, Kumar A, Lin H,  
557 Liu G, Liu X, Malguzzi P, Mallas I, Manoussakis M, Mastrangelo D, MacLachlan C,  
558 McLean P, Minami A, Mladek R, Nakazawa T, Najm S, Nie Y, Rixen M, Robertson  
559 AW, Ruti P, Sun C, Takaya Y, Tolstykh M, Venuti F, Waliser D, Woolnough S,  
560 Wu T, Won DJ, Xiao H, Zaripov R, Zhang L (2017) The subseasonal to seasonal  
561 (S2S) prediction project database. *Bulletin of the American Meteorological Society*  
562 98(1):163–173
- 563 Voldoire A, Decharme B, Pianezze J, Lebeaupin Brossier C, Sevault F, Seyfried  
564 L, Garnier V, Bielli S, Valcke S, Alias A, et al (2017) SURFEX v8. 0 inter-  
565 face with OASIS3-MCT to couple atmosphere with hydrology, ocean, waves and  
566 sea-ice models, from coastal to global scales. *Geoscientific Model Development*  
567 10(11):4207–4227
- 568 Voldoire A, Saint-Martin D, Sénési S, Decharme B, Alias A, Chevallier M, Colin J,  
569 Guérémy JF, Michou M, Moine MP, Nabat P, Roehrig R, Salas y Mélia D, Séférian  
570 R, Valcke S, Beau I, Belamari S, Berthet S, Cassou C, Cattiaux J, Deshayes J,  
571 H Douville H, Franchisteguy L, Ethé C, Geoffroy O, Lévy C, Madec G, Meurdesoif  
572 Y, Msadek R, Ribes A, Sanchez E, Terray L, Waldman R (2019) Evaluation of  
573 CMIP6 DECK experiments with CNRM-CM6-1. *Journal of Advances in Modeling*  
574 *Earth Systems* 11(7):2177–2213, DOI 10.1029/2019MS001683
- 575 Volonté A, Turner AG, Schiemann R, Vidale PL, Klingaman NP (2022) Characteris-  
576 ing the interaction of tropical and extratropical air masses controlling East Asian  
577 summer monsoon progression using a novel frontal detection approach. *Weather*  
578 *and Climate Dynamics* 3(2):575–599
- 579 Wilks DS (2011) *Statistical methods in the atmospheric sciences*, vol 100. Academic  
580 press
- 581 Xu L, Dirmeyer P (2013) Snow–atmosphere coupling strength. Part II: Albedo effect  
582 versus hydrological effect. *Journal of Hydrometeorology* 14(2):404–418
- 583 Xue Y, Oaida CM, Diallo I, Neelin JD, Li S, De Sales F, Gu Y, Robinson DA, Vasic R,  
584 Yi L (2016) Spring land temperature anomalies in northwestern us and the summer  
585 drought over southern plains and adjacent areas. *Environmental Research Letters*  
586 11(4):044018
- 587 Xue Y, Diallo I, Li W, David Neelin J, Chu PC, Vasic R, Guo W, Li Q, Robinson DA,  
588 Zhu Y, et al (2018) Spring land surface and subsurface temperature anomalies and  
589 subsequent downstream late spring-summer droughts/floods in north america and  
590 east asia. *Journal of Geophysical Research: Atmospheres* 123(10):5001–5019
- 591 Xue Y, Yao T, Boone AA, Diallo I, Liu Y, Zeng X, Lau WK, Sugimoto S, Tang Q,  
592 Pan X, et al (2021) Impact of initialized land surface temperature and snowpack  
593 on subseasonal to seasonal prediction project, phase I (LS4P-I): organization and  
594 experimental design. *Geoscientific Model Development* 14(7):4465–4494
- 595 Xue Y, Diallo I, Boone AA, Yao T, Zhang Y, Zeng X, Neelin JD, Lau WK, Pan  
596 Y, Liu Y, et al (2022) Spring Land Temperature in Tibetan Plateau and Global-  
597 Scale Summer Precipitation: Initialization and Improved Prediction. *Bulletin of the*  
598 *American Meteorological Society* 103(12):E2756–E2767
- 599 Xue Y, et al (2023) The remote effect of Tibetan Plateau spring land temperature on  
600 global subseasonal to seasonal precipitation prediction and the comparison with

- 601 sea surface temperature effect - The GEWEX/LS4P Phase I experiment. *Climate*  
602 *Dynamics*
- 603 Zhang C, Xie S, Klein SA, Ma Hy, Tang S, Van Weverberg K, Morcrette CJ, Petch  
604 J (2018) CAUSES: Diagnosis of the summertime warm bias in CMIP5 climate  
605 models at the ARM Southern Great Plains site. *Journal of Geophysical Research:*  
606 *Atmospheres* 123(6):2968–2992
- 607 Zhao C, Chen H, Sun S (2018) Evaluating the capabilities of soil enthalpy, soil  
608 moisture and soil temperature in predicting seasonal precipitation. *Advances in*  
609 *Atmospheric Sciences* 35:445–456
- 610 Zhou Y, Gao S, Shen SS (2004) A diagnostic study of formation and structures of the  
611 Meiyu front system over East Asia. *Journal of the Meteorological Society of Japan*  
612 *Ser II* 82(6):1565–1576

## 613 **5 Statements and Declarations**

614 This study was supported by the French national program LEFE (Les Enveloppes  
615 Fluides et l'Environnement).

616 The authors have no relevant financial or non-financial interests to disclose.

617 Both authors contributed to the study conception and design. Material preparation,  
618 data collection and analysis were performed by Constantin Ardilouze. Both authors  
619 wrote the first draft of the manuscript and commented on previous versions of the  
620 manuscript. Both authors read and approved the final manuscript.

621 ERA5 data (Hersbach, H. et al., 2018) was downloaded from the Copernicus  
622 Climate Change Service (C3S) (2023). The datasets generated during the current  
623 study are not publicly available but are available from the corresponding author on  
624 reasonable request